

This is a postprint version of the following published document:

Garcia-Gonzalez, D., Garzon-Hernandez, S., Rusinek, A., Bernier, R. & Arias, A. (2020). Low temperature mechanical behaviour of PVDF: cryogenic pre-treatment, quasi-static, cyclic and dynamic experimental testing and modelling. *Mechanics of Materials*, vol. 147, 103436.

DOI: [10.1016/j.mechmat.2020.103436](https://doi.org/10.1016/j.mechmat.2020.103436)

© 2020 Elsevier Ltd.



This work is licensed under a [Creative Commons Attribution-NonCommercial-NoDerivatives 4.0 International License](https://creativecommons.org/licenses/by-nc-nd/4.0/).

# Low temperature mechanical behaviour of PVDF: cryogenic pre-treatment, quasi-static, cyclic and dynamic experimental testing and modelling

D. Garcia-Gonzalez<sup>1,\*</sup>, S. Garzon-Hernandez<sup>1,2</sup>, A. Rusinek<sup>3,4</sup>, R. Bernier<sup>3</sup>, A. Arias<sup>1</sup>

<sup>1</sup> Department of Continuum Mechanics and Structural Analysis, University Carlos III of Madrid, Avda. de la Universidad 30, Leganés 28911, Madrid, Spain

<sup>2</sup> Department of Engineering Science, University of Oxford, Parks Road, Oxford OX1 3PJ, UK

<sup>3</sup> Laboratory of Microstructure Studies and Mechanics of Materials, UMR-CNRS 7239, Lorraine University, 7 rue Félix Savart, BP 15082, 57073, Metz Cedex 03, France

<sup>4</sup> Chair of Excellence, Departamento de Ingeniería Mecánica, Universidad Carlos III de Madrid, Avda. de la Universidad 30, 28911, Leganés, Madrid, Spain

\* Corresponding author: D. Garcia-Gonzalez, email address: [danigarc@ing.uc3m.es](mailto:danigarc@ing.uc3m.es)

**Abstract:** PVDF has historically drawn the interest of the scientific community because of its mechanical response to external stimuli. Recently, novel 3D printing techniques have been proposed to manufacture responsive PVDF components, leading to the reconsideration of this polymer in many applications (i.e., sensor-actuator or energy harvesting systems). During manufacturing and/or service conditions, PVDF structures can be subjected to large deformations that, eventually, can involve low temperature loading (e.g., piezoelectric sensors for aircrafts). In this work, a deep mechanical characterisation of PVDF specimens is carried out under low temperature conditions. To this end, we first evaluate potential effects of cryogenic pre-treatment going beyond the glass transition temperature of the polymer. Then, mechanical tests are conducted at different loading conditions and a wide range of testing temperatures from room to temperatures below glass transition: quasi-static compression tests, cyclic loading tests, and high strain rate tests. The complete set of experiments is analysed together to identify slow and fast relaxation mechanisms within the polymeric structure and motivate a new constitutive model. Finally, taking the experimental observations as formulation's basis, a thermodynamically consistent constitutive model is developed for finite deformations. This model describes the mechanical behaviour of PVDF as the combination of slow and fast response and accounts for strain rate dependency, temperature sensitivity, hysteresis and thermal evolution during the deformation process. The results from this work provide a full study of the mechanical behaviour of PVDF at low temperature, considering effects of both pre-treatment and testing temperature, and a new modelling tool to predict its response under a wide range of room-to-low temperature loading conditions.

## 1. Introduction

Polymeric materials have drawn the attention of both scientific and industrial communities to substitute metallic components as structural components within a wide variety of sectors such as aeronautical, automobile and biomedical industries (Schuhler et al., 2018; Garcia-Gonzalez et al., 2017; Garcia-Gonzalez and Landis, 2020). This interest has even increased with the possibility to introduce mechanical responses to external stimuli and *vice-versa* (smart polymers). In this regard, new polymeric materials are emerging to provide responsive structures to thermal gradients (Scalet et al., 2018), external magnetic fields (Kim et al., 2019; Garcia-Gonzalez et al., 2019) or electric stimulus (Yang et al., 2020). These materials are usually polymeric matrices filled with active particles that infer a mechanical response to the external stimulus such as magnetic particles embedded within a polymeric matrix (Kim et al., 2019). Other examples are based on elastomers that, combined with conductive

films, acquire capacitance-like properties which results into a coupled electro-mechanical behaviour (Liao et al., 2020). However, there are also some materials whose responsive behaviour is intrinsically linked to their own microstructure. Among these latter materials, polyvinylidene fluoride (PVDF) outstands because of its intrinsic mechanically responsive performance. PVDF is a semi-crystalline polymer with a rather complex molecular structure that can present up to five different crystalline phases. The most common phase is the  $\alpha$  one that consists of a non-polar phase with relevant applications within the chemical and oil industries (Castagnet et al., 2000). Starting from this non-polar  $\alpha$  phase, the PVDF material can be subjected to mechanical stretching leading to a reorientation of the polymeric chains forming a polar  $\beta$  phase with an associated dipole moment (Ruan et al., 2018; Li et al., 2014). This polar phase, as well as other phases with, but lower, dipole moment ( $\gamma$  and  $\delta$ ), can be alternatively obtained by application of high pressure, external electric field and ultra-fast cooling from melting conditions (Ruan et al., 2018). Hence, when PVDF has an internal polar microstructure, it presents pyroelectric and/or piezoelectric properties. Pyroelectricity is the property of some dielectric materials to experience a spontaneous electrical polarization against a temperature variation (Whatmore, 1991). Moreover, piezoelectricity is the property of a material to experience an electrical polarization against a mechanical deformation and *vice-versa* (Whatmore, 1991). The latter provides a wide range of possibilities to PVDF to be used as electromechanical sensor-actuator or for energy harvesting applications (Eddiai et al., 2019).

The  $\beta$  phase of PVDF has been used in interesting applications that focus on the transformation of mechanical to electrical signals for the design of sensors (Singh et al., 2020) or the transformation of electrical to mechanical signals for the design of actuators (Feng et al., 2017). The work by Dargaville et al. (2005) points out the interest from the National Aeronautics and Space Administration (NASA) to develop novel piezoelectric polymers for aircraft and aeronautical applications (Park et al., 2004). In such applications, the polymeric components will be exposed to huge thermal gradients along time that will go through the glass transition temperature (around  $-40^{\circ}\text{C}$ ) of the material. Thus, significant changes may be introduced within the polymeric microstructure leading to relevant changes in its macroscopic behaviour. In addition, the service conditions will cover a wide range of working temperatures from room to low ones and different loadings from quasi-static cycling to dynamic. Although not too much efforts have been done towards this direction, the appearance of novel 3D printing manufacturing techniques to produce PVDF in its  $\beta$  phase, open new avenues (Tarbuttona et al., 2017). Other applications working at cryogenic or low temperatures are polymer composites used for tribology or semiconductors (Baldissera and Delprete, 2013; Friedrich, 2018). Therefore, these applications need of a complete understanding of the mechanical behaviour of PVDF under low temperatures and different loading conditions as well as the evaluation of potential effects arising from the material exposition to significant thermal gradients.

Previous efforts to characterise and model the mechanical behaviour of PVDF can be found in the current literature. As an example, Siviour et al. (2005) performed an experimental campaign to test the mechanical response of PVDF under quasi-static and dynamic conditions at different testing temperatures. Furthermore, Motta et al. (2018) and Santimetaneedol et al. (2016) studied the mechanical response of PVDF under cyclic loading at room temperature. Other relevant works on the mechanical characterisation of PVDF can be found in Refs. (Haddadi et al., 2018; Zhang et al., 2019; Zhao et al., 2020). From all the experimental evidences to date, some conclusions can be stated: PVDF presents significant dependences on strain rate and temperature, this material can undergo large deformations combining elastic and inelastic components, and it presents clear hysteresis during cyclic loading. Moreover, different constitutive models have been proposed to describe the mechanical behaviour of PVDF (Vinogradov et al., 2004; Laiarinandrasana et al., 2009). However, to the authors' knowledge, there is still no combined experimental and modelling study covering the mechanical response of PVDF under different testing temperatures and testing conditions.

In this work, we analyse the influence of low temperature conditions on the mechanical response of PVDF from different perspectives. First, we evaluate possible effects due to previous cryogenic pre-treatments. This study aims at elucidating a potential dependence of the mechanical response of PVDF due to thermal history going far beyond its glass transition temperature. To this end, PVDF specimens without and with different cryogenic pre-treatments are tested at quasi-static, cyclic and dynamic loading conditions. Next, the mechanical behaviour of PVDF is experimentally studied at different temperatures from room temperature to  $-60^{\circ}\text{C}$ . This study covers a wide range of loading conditions to provide a complete view of the deformation mechanisms of PVDF: monotonic quasi-static loading conditions, cyclic loading conditions, and dynamic loading conditions. Then, the experimental observations are used to motivate the formulation of a new constitutive model to describe the main deformation mechanisms. This model is developed within a thermodynamically consistent framework for finite deformations and considers temperature dependences, strain rate sensitivity and hysteresis. Finally, the model is implemented and its parameters are identified to predict the mechanical response of PVDF, showing a good agreement with the experimental results and faithfully describing the different deformation mechanisms observed. Overall, a full study of the mechanical behaviour of PVDF at low temperature is presented, providing a new modelling tool to predict its response under a wide range of room-to-low temperature loading conditions. These results, along with future extensions of 3D printed polymeric modelling (Garzon-Hernandez et al., 2020), could potentially serve as basis for new avenues in 3D printed responsive components such as sensor-actuator systems.

## **2. Influence of cryogenic thermal pre-treatments on PVDF**

Before performing the characterisation tests to evaluate the effects of testing temperature, we analyse here potential alterations in the mechanical response of PVDF due to thermal pre-treatments. These tests aim at clarifying the suitability of this polymer to be used in aerospace or other applications where the components may be subjected to repetitive strong thermal gradients (i.e., biomedical, tribological). In this regard, the glass transition of PVDF is found around  $-40^{\circ}\text{C}$ . Above this temperature, a relevant relaxation process occurs within the polymer leading to higher mobility of the molecular chains. On contrary, temperatures below this point result into a stiffened microstructure with lower mobility between polymeric chains. The experiments conducted in this work aim to elucidate potential effects of cryogenic conditions on PVDF considering two main aspects: cryogenic cycles and magnitude of the cryogenic temperature. The first case can be experienced, for instance, in PVDF sensors used in aeronautical applications where they are subjected to low temperatures during flying conditions and moderate temperatures while landed. The second case is representative, for instance, of aerospace applications. Therefore, in order to study potential residual effects arising from cyclic thermal loading, we have prepared four different groups of cylindrical PVDF specimens with dimensions 8 mm in diameter and 4 mm in height: (i) specimens without thermal treatment; (ii) specimens subjected to  $-80^{\circ}\text{C}$  during 12h; (iii) specimens subjected to  $-175^{\circ}\text{C}$  during 8h; (iv) specimens subjected to two cycles of  $-80^{\circ}\text{C}$  during 12h. These temperatures are representative of cryogenic processing for permanent treatment of the materials as well as aeronautical and aerospace environments. Then, the four groups of thermally pre-treated specimens were tested under different compression loading conditions: quasi-static loading, cyclic loading and dynamic loading. The quasi-static monotonic and cyclic tests were conducted with a universal testing machine, while the dynamic tests were conducted with a split Hopkinson pressure bar (SHPB). A scheme of these experimental setups used for these tests is shown in Figure 1.

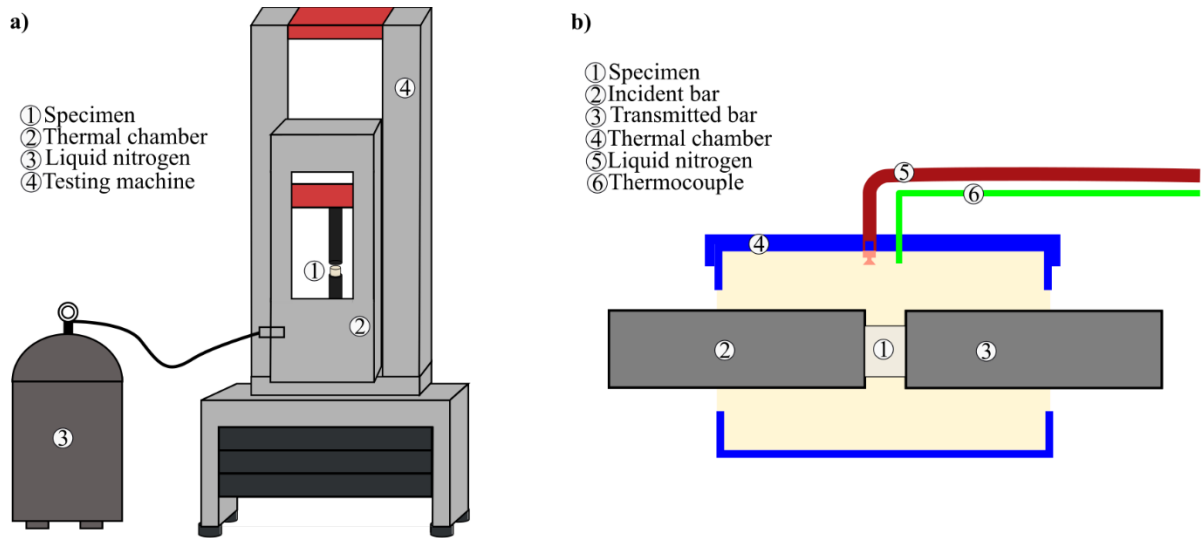


**Figure 1:** Schemes of the experimental setups used for: a) uniaxial monotonic and cyclic tests (universal testing machine); b) dynamic compression tests (SHPB).

### *Quasi-static loading conditions*

Uniaxial monotonic compression tests were conducted for a strain rate of  $0.001 \text{ s}^{-1}$ . A total number of 3 specimens per conditions were tested to obtain reliable results. These experiments were performed in a universal testing machine. The cylindrical faces in contact with the compression plates were lubricated to keep longer the strain uniformity and improve uniaxial conditions.

The mechanical results obtained for the different thermal treatments are shown in Figure 2. It seems that the thermal treatments influence the stress flow at large deformations, but these changes are not significant under quasi-static loading.

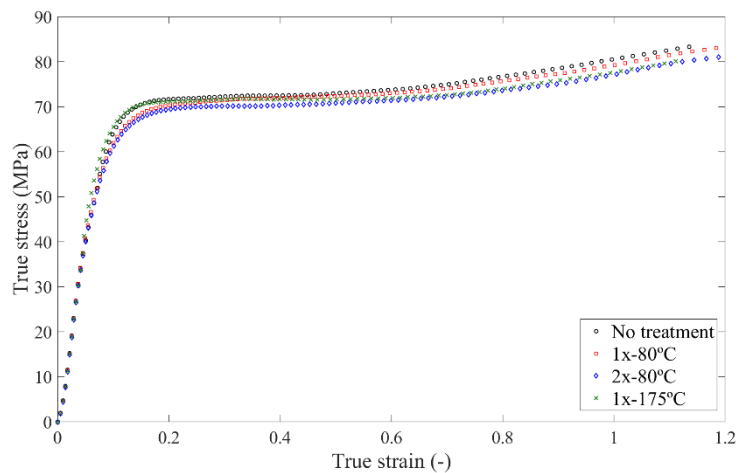


**Figure 2:** Comparison of the mechanical behaviour under compression quasi-static loading ( $0.001 \text{ s}^{-1}$ ) of PVDF specimens with different thermal pre-treatments: without thermal treatment; subjected to  $-80^\circ\text{C}$  during 12h; subjected to  $-175^\circ\text{C}$  during 8h; subjected to two cycles of  $-80^\circ\text{C}$  during 12h.

### *Cyclic loading conditions*

Uniaxial compression tests under cyclic loading were conducted to analyse potential effects of the thermal history on both the strain rate sensitivity of PVDF and its hysteresis response. A total number of 3 specimens per conditions were tested to obtain reliable results. These experiments were performed in the same testing machine used for the monotonic loading. The cylindrical faces in contact with the compression plates were also lubricated to keep longer the strain uniformity and improve uniaxial conditions. These tests consist of a number of 6 cycles to a true deformation around 18% and a final loading until large true deformations around 120%. During these tests, the strain rate was kept constant to  $0.01 \text{ s}^{-1}$ .

The mechanical results obtained for the different thermal treatments are shown in Figure 3. This figure shows the mechanical response of the specimens during the whole loading process as well as a detailed presentation of the hysteresis loops. Important permanent deformation is observed after the first hysteresis loop. After the second hysteresis loop, a significant increase in permanent deformation is noted and, from the third loop the material response is not further modified. These results are rather similar to Mullins' effect in other type of polymers. Note that no relevant differences are observed between specimens with and without thermal pre-treatments.

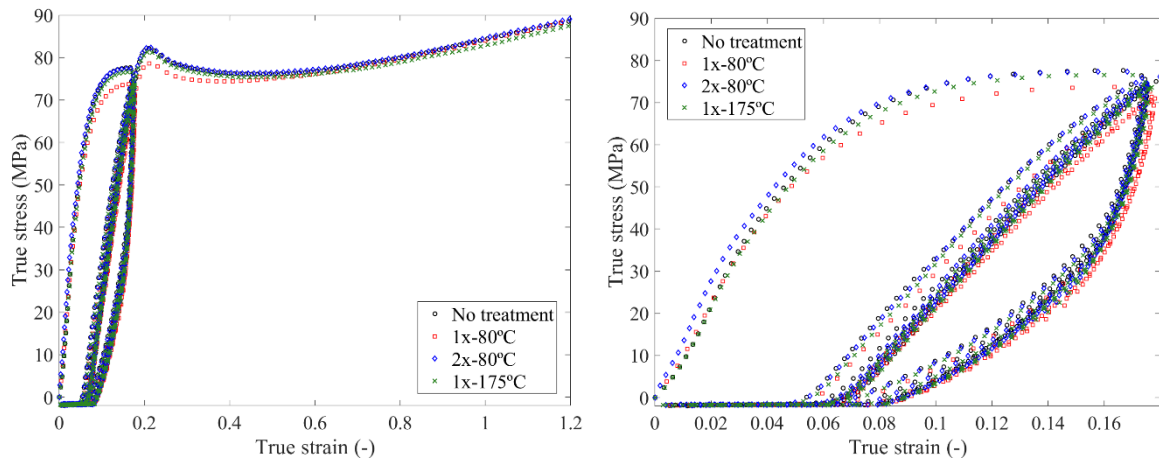


**Figure 3:** Comparison of the mechanical behaviour under compression quasi-static cycling loading ( $0.01 \text{ s}^{-1}$ ) of PVDF specimens with different thermal pre-treatments: without thermal treatment; subjected to  $-80^{\circ}\text{C}$  during 12h; subjected to  $-175^{\circ}\text{C}$  during 8h; subjected to two cycles of  $-80^{\circ}\text{C}$  during 12h.

### *Dynamic loading conditions*

Finally, potential effects of the thermal history on the dynamic response of PVDF were studied. To this end, compression tests were performed using a SHPB for dynamic conditions at high strain rates. A total number of 3 specimens per conditions were tested to obtain reliable results. The cylindrical faces in contact with the impact and transmitted bars were lubricated to keep longer the strain uniformity and improve uniaxial conditions. These tests were conducted for an average strain rate of  $2000 \text{ s}^{-1}$ .

The stress-strain curves obtained for the different thermal treatments are shown in Figure 4. This figure shows almost identical mechanical response of the different PVDF specimens to dynamic loading, indicating no influence of the thermal treatments considered on its behaviour.



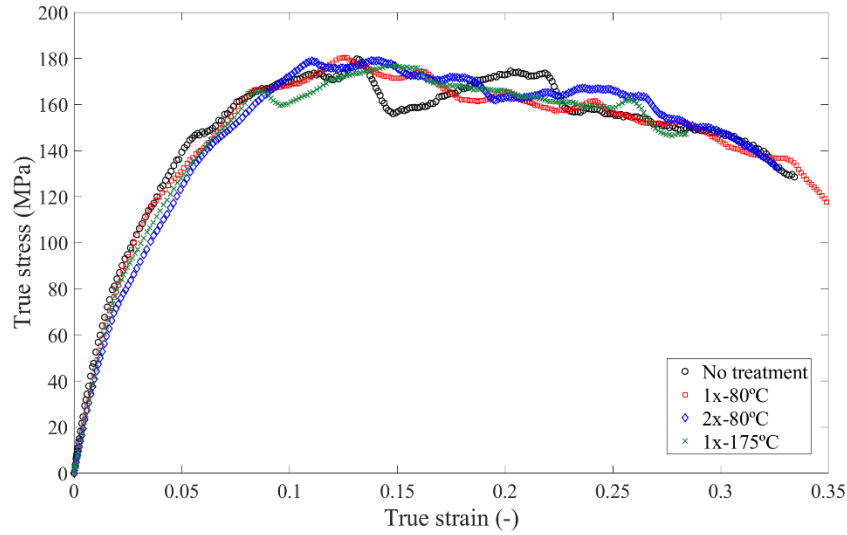


**Figure 4:** Comparison of the mechanical behaviour under compression dynamic loading ( $2000 \text{ s}^{-1}$ ) of PVDF specimens with different thermal pre-treatments: without thermal treatment; subjected to  $-80^{\circ}\text{C}$  during 12h; subjected to  $-175^{\circ}\text{C}$  during 8h; subjected to two cycles of  $-80^{\circ}\text{C}$  during 12h.

Therefore, it can be concluded that the mechanical response of PVDF under compression loading does not depend on the previous low-temperature thermal history, even if cryogenic temperatures are reached. However, low temperatures along with mechanical loading can significantly alter the response of PVDF. These influences are studied next.

### 3. Influence of thermal testing conditions on PVDF

In this section, we provide a detailed characterisation of the mechanical response of PVDF to analyse potential dependences at low testing temperatures and different loading conditions. All these tests are performed on specimens without thermal pre-treatments.

#### 3.1. Quasi-static loading conditions

Uniaxial monotonic compression tests were conducted for a strain rate of  $0.001 \text{ s}^{-1}$  and following the methods described above to compare PVDF specimens with thermal treatments. In addition, a thermal chamber connected to a liquid nitrogen supplier was incorporated to the universal testing machine. Thus, cryogenic gas is supplied into the chamber fixed around the specimen allowing for a uniform temperature. The temperature is controlled by monitoring via a thermocouple. In all cases, we wait for 30 min to ensure uniform temperature within the specimen. Following this method, the testing temperature was modified during the experimental program to provide a wide range from room temperature to  $-60^{\circ}\text{C}$ , considering values below and above the glass transition.

The experimental results for these tests are shown in Figure 5. In this figure, a clear stiffening of the polymer with the decrease in temperature can be appreciated. This thermal dependence can be observed by means of Young's modulus and yield stress. In this regard, there is a strong jump in material properties when crossing the glass transition temperature ( $-40^{\circ}\text{C}$ ). Within this regime, the polymeric chains suffer a reduction in mobility resulting in a significant increase of stiffness. Furthermore, a decrease in molecular chains' locking stretch with decreasing temperature is intuited according to the flow stress evolution after yielding. Our interpretation suggests a loss in the stretch capacity of the polymeric chains for lower testing temperatures leading to asymptotic tendencies in stress for lower deformation levels. These observations can also be understood, from a macrostructural point of view, as higher deformation hardening at low temperatures.

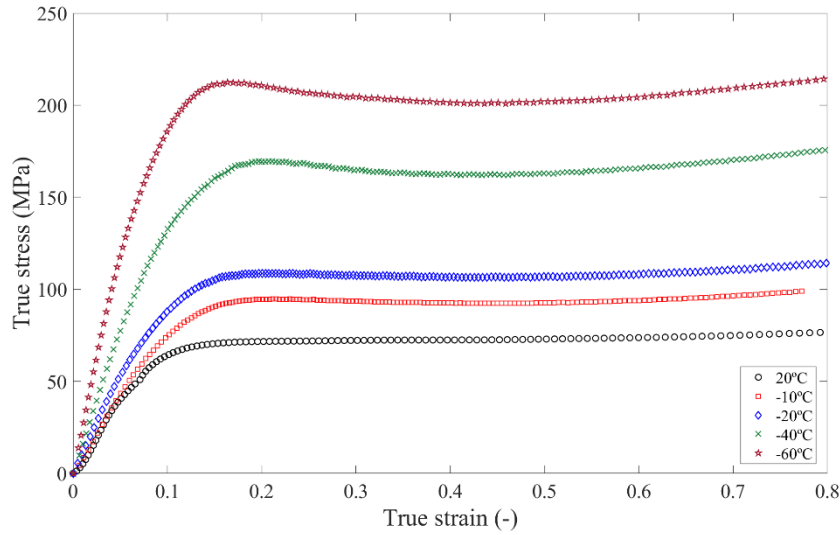


**Figure 5:** Mechanical behaviour under compression quasi-static loading ( $0.001 \text{ s}^{-1}$ ) of PVDF specimens at different temperatures: room,  $-10^\circ\text{C}$ ,  $-20^\circ\text{C}$ ,  $-40^\circ\text{C}$ ,  $-60^\circ\text{C}$ .

### 3.2. Cyclic loading conditions

Uniaxial cyclic compression tests (up to 6 cycles) were conducted with a mean strain rate of  $0.01 \text{ s}^{-1}$  and following the methods described above to compare PVDF specimens with thermal treatments. These tests allow for evaluating strain rates effects within the quasi-static regime and hysteresis responses. For these tests, the thermal chamber with the nitrogen supplier is connected. The temperature is controlled as done for the monotonic tests applying a waiting time of 30 min to ensure uniform temperature within the specimen. The testing temperature was changed from room temperature to  $-60^\circ\text{C}$ , considering values below and above the glass transition.

The experimental results for these tests are shown in Figure 6. These results present similar tendencies than in monotonic loading by means of yield stress and Young's modulus. In addition, the hysteresis loops are consistent with these tendencies. A Mullins' like effect is observed where the hysteresis loops stabilised at the second/third cycle. Moreover, flatter flow stresses are found at higher temperatures, suggesting higher deformation hardening associated to an increase in polymeric chains' mobility with testing temperature (and *vice versa*). This effect is more pronounced when going across the glass transition, being consistent with the theoretical microstructural changes.

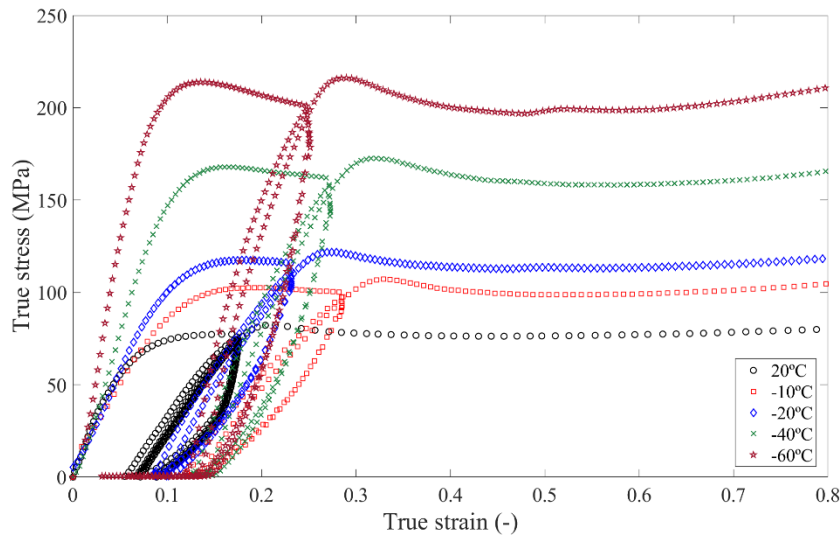




**Figure 6:** Mechanical behaviour under compression cyclic loading ( $0.01 \text{ s}^{-1}$ ) of PVDF specimens at different temperatures: room,  $-10^{\circ}\text{C}$ ,  $-20^{\circ}\text{C}$ ,  $-40^{\circ}\text{C}$ ,  $-60^{\circ}\text{C}$ .

### 3.3. Dynamic loading conditions

Dynamic compression tests were conducted with a mean strain rate of  $2000 \text{ s}^{-1}$  and following the methods described above to compare PVDF specimens with thermal treatments. These tests allow for evaluating strain rates effects within the dynamic regime and identifying transitions in the failure mode of PVDF. For these tests, the thermal chamber with the nitrogen supplier is incorporated to the SHPB setup. A waiting time of 30 min is used to ensure uniform temperature within the specimen. The testing temperature was changed from room temperature to  $-60^{\circ}\text{C}$ , considering values below and above the glass transition.

These results are shown in Figure 7. Analysing the maximum stresses reached, two different tendencies can be identified. At testing temperatures from  $-10^{\circ}\text{C}$  to higher values, an increase in temperature results into lower maximum stresses reached. However, from  $-20^{\circ}\text{C}$  to lower values, the maximum stress peak decreases for lower temperatures. This change in tendency is explained by a transition in the failure mechanisms experienced by PVDF that strongly affects its ductility. A fully ductile behaviour is observed at room temperature, where the polymer undergoes large deformations without showing any sign of fracture. When the testing temperature is decreased, we find a reduction in PVDF ductility in a slight transition to brittle failure. This transition can be observed for specimens tested at  $-10^{\circ}\text{C}$  and  $-20^{\circ}\text{C}$  where the PVDF undergoes significant fractures. This brittleness becomes even more relevant when reaching the glass transition. The images provided in Figure 7 for the tests at  $-40^{\circ}\text{C}$  and  $-60^{\circ}\text{C}$  show a completely brittle behaviour that results into multiple fracture within the whole specimen. From a microstructural perspective, the reduction in polymeric chains' mobility hinders the polymer deformation and relative movement of these chains, leading to the brittleness in the macroscopic failure. This macroscopic failure can be understood as a competition between ductile and brittle fracture mechanisms, each one defined by a stress threshold. The fracture mode is determined by which threshold is first reached. In this regard, the brittle fracture is governed by a brittle strength (stress threshold) associated to material imperfections that are, *a priori*, not dependent on strain rate and temperature. Moreover, the ductile threshold is associated to the yield stress that, as shown before, strongly depends on strain rate and temperature. Therefore, when increasing strain rate and decreasing testing temperature, the polymer experiences a strong increase in yield stress adopting values above the brittle strength. In such cases, the brittle threshold is first reached leading to the completely brittle fracture of PVDF and changing the trend in maximum stress versus testing temperature.

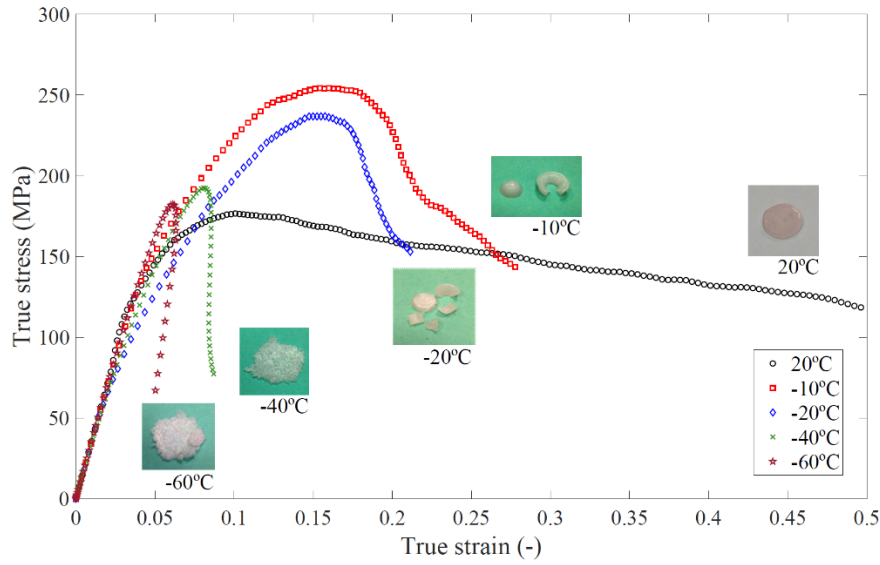


**Figure 7:** Mechanical behaviour under compression dynamic loading ( $2000 \text{ s}^{-1}$ ) of PVDF specimens at different temperatures: room,  $-10^\circ\text{C}$ ,  $-20^\circ\text{C}$ ,  $-40^\circ\text{C}$ ,  $-60^\circ\text{C}$ .

Finally, to provide an overall view of the experimental results and the influence of testing temperature on PVDF at different strain rates, the maximum stresses reached for each test condition are shown together in Figure 8. The experimental results have been divided into sets of data below and above glass transition. Then, linear fitting is used to provide the peak stress-temperature tendencies at the different strain rates tested below and above glass transition. The experiments at low strain rate show a considerable change in the peak stress-temperature slope when crossing such transition. Moreover, experiments at high strain rate show an even clearer change in material response, which is mainly governed by a transition from ductile to brittle failure (see Figure 7 for material fracture). Note that the ductile-to-brittle transition of the polymer is intimately coupled to both temperature and strain rate and can be moved to higher temperatures with an increase of strain rate. In addition, note that two main viscous dependences can be inferred from the experiments conducted: slow relaxation governing the hysteresis loops at low strain rates; and a fast response governing the hardening due to strain rate sensitivity at high strain rates. These slow and fast responses will be taken into account next to model the mechanical behaviour of PDVF.

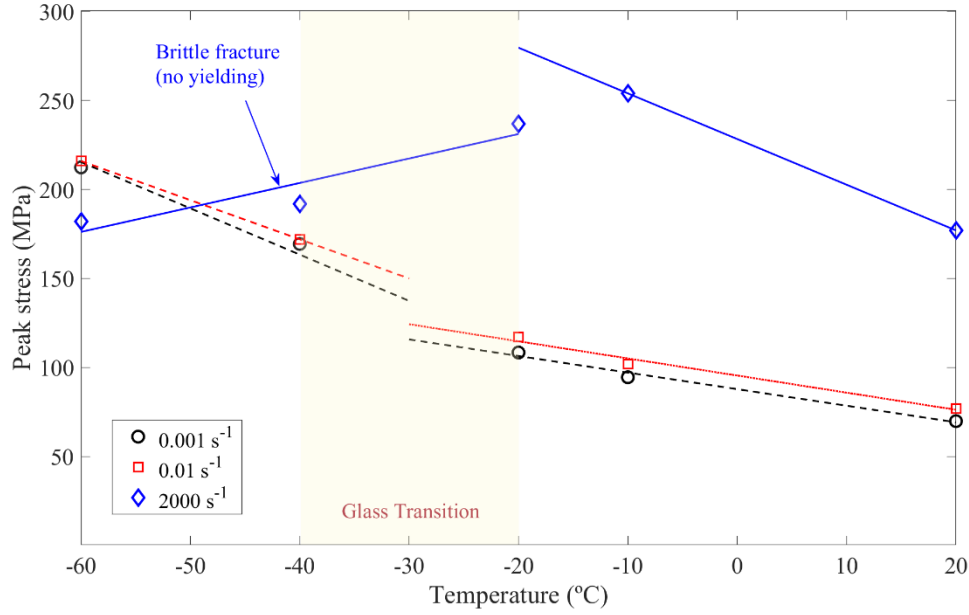


**Figure 8:** Peak stress versus testing temperature of PVDF at different strain rate conditions. Peak stress refers to yield stress in ductile specimens and ultimate strength in brittle specimens.

#### 4. Constitutive modelling

A new constitutive model to describe the different thermo-mechanical dependences observed during the experiments is proposed. The mechanical behaviour of PVDF presents a strong dependence on strain rate leading to a relevant hardening by means of yield and flow stresses. Furthermore, the material response is highly sensitive to testing temperature, affecting both initial stiffness and yielding. This temperature dependence is also relevant during mechanical deformation where inelastic dissipation results into heating and, consequently, into mechanical softening. In addition, other rate dependences are observed in the form of viscous relaxation mechanisms leading to hysteresis in the stress-deformation curves. All these experimental observations and material dependences are coupled together within a thermodynamically consistent constitutive model formulated for finite deformations. Note that the proposed model, although focused on PVDF, aims at being general and provides the basis for further particularisation to other semi-crystalline polymers.

In this section, we first introduce the basis of the formulation and the associated kinematics. Then, the thermodynamic context is presented and the constitutive relations as well as temperature evolution during the deformation process are derived accordingly. Finally, specific energy functions and flow rules are given.

##### 4.1. Model basis and kinematics

The model takes its basis from the assumption of two visco-hyperelastic components acting in parallel. The first component relates to a fast relaxation response whereas the second component is associated to a slow relaxation response guided by a back-stress softened with viscous flow. Therefore, the fast relaxation contribution is the responsible (major player) for the instantaneous response of the material by means of strain rate dependence. This component is hypothesised to describe the intermolecular resistance to deformation. Moreover, the slow relaxation aims at describing the polymeric network accompanied by a softening potentially arising from detangling or melting of network junctions. This approach has previously been used by Li et al. (2019) to model the mechanical behaviour of another semi-crystalline polymer (PEEK). The mechanical description is completed with a third resistance associated to volumetric deformation. In addition, thermal dependences are added to these resistances

to introduce temperature sensitivity and allows for describing the softening caused by inelastic dissipation during the deformation process.

A rheological scheme of the model representing the different resistances to deformation is shown in Figure 9. Here, the overall response of the material is split into volumetric ( $\sigma_{vol}$ ) and isochoric ( $\sigma_{iso}$ ) contributions leading to a total Cauchy stress tensor  $\sigma$  as:

$$\sigma = \sigma_{vol} + \sigma_{iso} \quad (1)$$

where the isochoric contribution is the sum of both fast ( $\sigma_f$ ) and slow ( $\sigma_s$ ) relaxation branches:

$$\sigma_{iso} = \sigma_f + \sigma_s \quad (2)$$

The slow relaxation contribution, in turn, can be defined by the Cauchy stress tensor associated to each rheological component of the constitutive branch as:

$$\sigma_s = \sigma_s^{ev} + \sigma_s^{flow} \quad (3)$$

where  $\sigma_s^{ev}$  is the stress acting on the non-linear spring in parallel with the dashpot and  $\sigma_s^{flow}$  is the stress driving the viscous flow.

Moreover, the total deformation gradient  $\mathbf{F}$  can be decomposed, depending on the corresponding constitutive branch as:

$$\mathbf{F} = \mathbf{F}_f^e \mathbf{F}_f^v \mathbf{F}_{vol} = \mathbf{F}_s^e \mathbf{F}_s^v \mathbf{F}_{vol} \quad (4)$$

with  $\mathbf{F}_{vol} = J^{1/3} \mathbf{I}$  being the volumetric deformation gradient with  $J = \det(\mathbf{F})$ ;  $\mathbf{F}_f^e$  and  $\mathbf{F}_f^v$  the elastic and viscous components of the fast relaxation deformation gradient, respectively; and  $\mathbf{F}_s^e$  and  $\mathbf{F}_s^v$  the elastic and viscous components of the slow relaxation deformation gradient, respectively.

To help the constitutive formulation of the model, three intermediate configurations are included (see Figure 9). Thus, the current or deformed configuration can be reached from the reference or undeformed configuration by use of the total deformation gradient  $\mathbf{F}$ . Furthermore, the intermediate configuration  $\bar{\Omega}$  denoted as dilated configuration is given by the unique application of the volumetric deformation gradient. Finally, the two relaxed dilated configurations  $\bar{\Omega}$  and  $\bar{\bar{\Omega}}$  can be reached from the dilated configuration by the application of the viscous components of the deformation gradient  $\mathbf{F}_s^v$  and  $\mathbf{F}_f^v$ , respectively. Therefore, the spatial velocity gradient  $\mathbf{L}$ , depending on the constitutive branch, is given by:

$$\mathbf{L} = \dot{\mathbf{F}} \mathbf{F}^{-1} = \mathbf{L}_{vol} + \mathbf{L}_f^e + \mathbf{L}_f^v = \mathbf{F}_f^e \mathbf{F}_f^v \dot{\mathbf{F}}_{vol} \mathbf{F}_{vol}^{-1} \mathbf{F}_f^{v-1} \mathbf{F}_f^{e-1} + \dot{\mathbf{F}}_f^e \mathbf{F}_f^{e-1} + \mathbf{F}_f^e \dot{\mathbf{F}}_f^v \mathbf{F}_f^{v-1} \mathbf{F}_f^{e-1} \quad (5.1)$$

$$\mathbf{L} = \dot{\mathbf{F}} \mathbf{F}^{-1} = \mathbf{L}_{vol} + \mathbf{L}_s^e + \mathbf{L}_s^v = \mathbf{F}_s^e \mathbf{F}_s^v \dot{\mathbf{F}}_{vol} \mathbf{F}_{vol}^{-1} \mathbf{F}_s^{v-1} \mathbf{F}_s^{e-1} + \dot{\mathbf{F}}_s^e \mathbf{F}_s^{e-1} + \mathbf{F}_s^e \dot{\mathbf{F}}_s^v \mathbf{F}_s^{v-1} \mathbf{F}_s^{e-1} \quad (5.2)$$

with  $\mathbf{L}_{vol}$  being the volumetric component;  $\mathbf{L}_f^e$  and  $\mathbf{L}_s^e$  the elastic components of the fast and slow relaxation components, respectively; and  $\mathbf{L}_f^v = \mathbf{D}_f^v + \mathbf{W}_f^v$  and  $\mathbf{L}_s^v = \mathbf{D}_s^v + \mathbf{W}_s^v$  the viscous components of the fast and slow relaxation components, respectively, where  $\mathbf{D}_i^v = \frac{1}{2}(\mathbf{L}_i^v + \mathbf{L}_i^{vT})$  and  $\mathbf{W}_i^v = \frac{1}{2}(\mathbf{L}_i^v - \mathbf{L}_i^{vT})$ . The proposed model assumes null viscous rotations so that  $\mathbf{W}_i^v = \mathbf{0}$ .

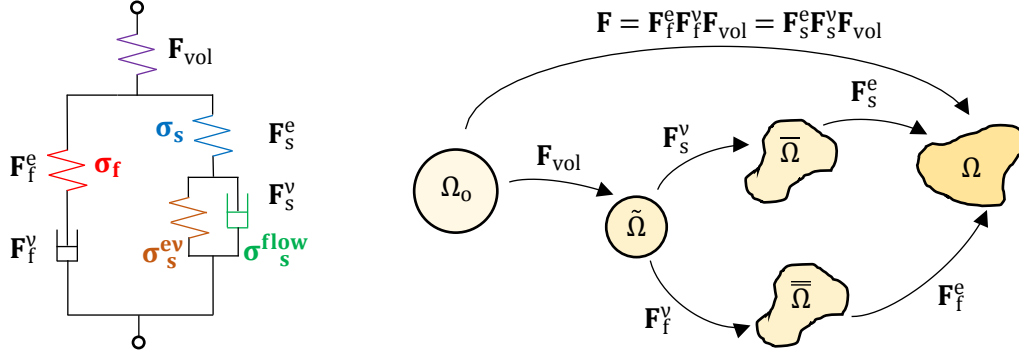


**Figure 9:** Rheological scheme of the model (left) and the corresponding kinematics (right).

## 4.2. Thermodynamics

The thermo-mechanical behaviour of the material is defined by a total Helmholtz free energy function per unit reference volume  $\Psi(\mathbf{F}, \mathbf{F}_f^v, \mathbf{F}_s^v, T)$  that depends on the total deformation gradient, the temperature and two internal variables corresponding to the viscous contributions from both relaxation branches. Thus, this total energy potential can be decomposed in a volumetric component  $\Psi_{vol}(\mathbf{F})$ ; a fast relaxation component  $\Psi_f(\mathbf{F}, \mathbf{F}_f^v, T)$ ; a slow relaxation component  $\Psi_s(\mathbf{F}, \mathbf{F}_s^v, T)$ ; and a thermal component  $\Psi_t(T)$  as:

$$\Psi(\mathbf{F}, \mathbf{F}_f^v, \mathbf{F}_s^v, T) = \Psi_{vol}(\mathbf{F}) + \Psi_f(\mathbf{F}, \mathbf{F}_f^v, T) + \Psi_s(\mathbf{F}, \mathbf{F}_s^v, T) + \Psi_t(T) \quad (6)$$

Note that the total energy function can be rewritten, for convenience, depending on the elastic deformation gradients as  $\Psi(\mathbf{F}, \mathbf{F}_f^e, \mathbf{F}_s^e, T)$  and, therefore,  $\Psi_f(\mathbf{F}, \mathbf{F}_f^v, T) = \Psi_f(\mathbf{F}_f^e, T)$  and  $\Psi_s(\mathbf{F}, \mathbf{F}_s^v, T) = \Psi_s(\mathbf{F}_s^e, T)$ . In addition, note that an energy potential  $\Psi_s^v(\mathbf{F}_s^v, T)$  can be associated to the spring of the slow relaxation branch in parallel to the dashpot. This energy potential will determine the stress contribution acting on such spring and its contribution is already accounted within the energy potential  $\Psi_s$ .

Combining the first and second Principles of Thermodynamics with the definition of the Helmholtz free energy given in Eq. (6), we reach the following expression for the Clausius-Plank inequality (see Garcia-Gonzalez and Jerusalem (2019) for more details):

$$\mathcal{D}_{int} = \left[ \mathbf{P} - J \frac{\partial \Psi_{vol}}{\partial \mathbf{F}} \mathbf{F}^{-T} - J^{-\frac{1}{3}} \mathbb{P} : \left( \frac{\partial \Psi_f}{\partial \mathbf{F}_f^v} \mathbf{F}_f^v \mathbf{F}_f^{-T} + \frac{\partial \Psi_s}{\partial \mathbf{F}_s^v} \mathbf{F}_s^v \mathbf{F}_s^{-T} \right) \right] : \dot{\mathbf{F}} - \left[ \eta + \frac{\partial \Psi}{\partial T} \right] \dot{T} + \frac{\partial \Psi_f}{\partial \mathbf{F}_f^e} : \mathbf{F}_f^e \dot{\mathbf{F}}_f^v \mathbf{F}_f^{-T} + \frac{\partial \Psi_s}{\partial \mathbf{F}_s^e} : \mathbf{F}_s^e \dot{\mathbf{F}}_s^v \mathbf{F}_s^{-T} \geq 0 \quad (7)$$

where  $\mathbf{P}$  is the first Piola-Kirchhoff stress,  $\mathbb{P} = \mathbb{I} - \frac{1}{3} \mathbf{F}^{-T} \otimes \mathbf{F}$  defines a fourth-order projection tensor with  $\mathbf{F}$  operating as a metric tensor, with  $\mathbb{I}$  denotes a fourth-order unity tensor, and  $\eta$  is the specific entropy per unit reference volume. The standard Coleman-Noll procedure (Coleman and Noll, 1963; Coleman and Gurtin, 1967) can be applied to satisfy this inequality for any given deformation and, thus, the constitutive relations are consistently obtained:

$$\mathbf{P} = \frac{\partial \Psi}{\partial \mathbf{F}} = J \frac{\partial \Psi_{vol}}{\partial \mathbf{F}} \mathbf{F}^{-T} + J^{-\frac{1}{3}} \mathbb{P} : \left( \frac{\partial \Psi_f}{\partial \mathbf{F}_f^v} \mathbf{F}_f^v \mathbf{F}_f^{-T} + \frac{\partial \Psi_s}{\partial \mathbf{F}_s^v} \mathbf{F}_s^v \mathbf{F}_s^{-T} \right) \quad (8.1)$$

$$\eta = - \frac{\partial \Psi}{\partial T} \quad (8.2)$$

The first Piola-Kirchhoff stress tensor can be split into different components associated to each constitutive branch as:

$$\mathbf{P} = \mathbf{P}_{\text{vol}} + \mathbf{P}_f + \mathbf{P}_s \quad (9)$$

where  $\mathbf{P}_{\text{vol}}$  is the volumetric component,  $\mathbf{P}_f$  is the fast relaxation component and  $\mathbf{P}_s$  is the slow relaxation component. These stress tensors are given by the following relations with the energy potentials:

$$\mathbf{P}_{\text{vol}} = J \frac{\partial \Psi_{\text{vol}}}{\partial J} \mathbf{F}^{-T} \quad (10.1)$$

$$\mathbf{P}_f = J^{-\frac{1}{3}} \mathbb{P} : \frac{\partial \Psi_f}{\partial \mathbf{F}_f^e} \mathbf{F}_f^v \mathbf{F}_f^{-T} \quad (10.2)$$

$$\mathbf{P}_s = J^{-\frac{1}{3}} \mathbb{P} : \frac{\partial \Psi_s}{\partial \mathbf{F}_s^e} \mathbf{F}_s^v \mathbf{F}_s^{-T} \quad (10.3)$$

Note that the first Piola-Kirchhoff stress tensors can be related with their corresponding Cauchy stress tensors by  $\boldsymbol{\sigma} = J^{-1} \mathbf{P} \mathbf{F}^T$ .

The last two terms in Eq. (7) refer to the viscous dissipation of the fast and slow relaxation mechanisms, respectively. In this regard, consistent viscous flow rules must be defined to satisfy the thermodynamic conditions:

$$\frac{\partial \Psi_f}{\partial \mathbf{F}_f^e} : \mathbf{F}_f^e \dot{\mathbf{F}}_f^v \mathbf{F}_f^{-T} \geq 0 \quad (11.1)$$

$$\frac{\partial \Psi_s}{\partial \mathbf{F}_s^e} : \mathbf{F}_s^e \dot{\mathbf{F}}_s^v \mathbf{F}_s^{-T} \geq 0 \quad (11.2)$$

Finally, following the procedure used by Refs. (Garcia-Gonzalez et al., 2017; Barba et al., 2020; Garcia-Gonzalez et al., 2020) and neglecting thermoelastic contributions, the evolution of the temperature during the deformation process reads:

$$C \dot{T} = \beta (\boldsymbol{\sigma}_f^{\text{dev}} : \mathbf{D}_f^v + \boldsymbol{\sigma}_s^{\text{dev}} : \mathbf{D}_s^v) - \text{Div}(\mathbf{Q}) \quad (12)$$

where  $\boldsymbol{\sigma}_i^{\text{dev}}$  are the deviatoric components of the corresponding Cauchy stress tensor,  $-\text{Div}(\mathbf{Q})$  represents heat conduction (with  $\mathbf{Q}$  being the heat flux per unit area),  $C$  represents the specific heat and  $\beta$  is the Quinney–Taylor heat fraction coefficient. [Other relevant approaches to consistently compute temperature evolution during inelastic deformation processes can be found in Refs. \(Yu et al., 2017; Shen et al., 2019\).](#)

### 4.3. Specific Helmholtz free energy functions and stress tensors

Once the constitutive framework is complete, we need to provide specific energy functions to allow for the derivation of the stress tensors. The volumetric contribution is defined as:

$$\Psi_{\text{vol}}(\mathbf{F}) = K(J - 1)^2 \quad (13)$$

where  $K$  is the bulk modulus of the material.

The energy function of the fast relaxation response is defined by a Neo-Hookean model as:

$$\Psi_f(\mathbf{F}_f^e, T) = \frac{\mu_f(T)}{2} (I_f^e - 3) \quad (14)$$

where  $\mu_f(T)$  is the temperature-dependent shear modulus of this resistance, and  $I_f^e = \text{tr}(\mathbf{F}_f^{eT} \mathbf{F}_f^e)$ .



Similarly, the total energy function of the slow relaxation response is defined by a Neo-Hookean model as:

$$\Psi_s(\mathbf{F}_s^e, T) = \frac{\mu_s(T)}{2} (I_s^e - 3) \quad (15)$$

where  $\mu_s(T)$  is the temperature-dependent shear modulus of this resistance, and  $I_s^e = \text{tr}(\mathbf{F}_s^{eT} \mathbf{F}_s^e)$ .

In addition, the slow relaxation response needs the definition of the free energy associated to the viscous deformation  $\Psi_s^v(\mathbf{F}_s^v, T)$ . The modification of the original eight-chain model (Arruda and Boyce, 1993) proposed by Anand et al. (1996) is used:

$$\Psi_s^v(\mathbf{F}_s^v, T) = \mu_{sv}(T) \bar{\lambda}_L^2 \left\{ \frac{\bar{\lambda}^v}{\bar{\lambda}_L} \mathfrak{L}^{-1} \left( \frac{\bar{\lambda}^v}{\bar{\lambda}_L} \right) + \ln \left[ \frac{\mathfrak{L}^{-1} \left( \frac{\bar{\lambda}^v}{\bar{\lambda}_L} \right)}{\sinh \left[ \mathfrak{L}^{-1} \left( \frac{\bar{\lambda}^v}{\bar{\lambda}_L} \right) \right]} \right] \right\} \quad (16)$$

where  $\mu_{sv}(T)$  is the temperature-dependent shear modulus of this resistance,  $\bar{\lambda}_L$  is the locking stretch of the polymeric chains,  $\mathfrak{L}^{-1}$  is the inverse of the Langevin function and  $\bar{\lambda}^v = \sqrt{\frac{1}{3} \text{tr}(\mathbf{F}_s^v \mathbf{F}_s^{vT})}$  is the average total stretch ratio.

The constitutive equations that provide the total Cauchy stress tensor are given by Eqs. (10) and (13)-(15) along with its transformation from Piola-Kirchhoff stress tensor. Making use of these expressions we reach:

$$\boldsymbol{\sigma}_{\text{vol}} = K(J - 1) \mathbf{I} \quad (17.1)$$

$$\boldsymbol{\sigma}_f = \frac{\mu_f(T)}{J} (\mathbf{B}_f^e)^{\text{dev}} \quad (17.2)$$

$$\boldsymbol{\sigma}_s = \frac{\mu_s(T)}{J} (\mathbf{B}_s^e)^{\text{dev}} \quad (17.3)$$

where  $(\mathbf{B}_f^e)^{\text{dev}}$  and  $(\mathbf{B}_s^e)^{\text{dev}}$  are the deviatoric parts of the left Cauchy-Green deformation tensors  $\mathbf{B}_f^e = \mathbf{F}_f^e \mathbf{F}_f^{eT}$  and  $\mathbf{B}_s^e = \mathbf{F}_s^e \mathbf{F}_s^{eT}$ . Similarly, the Cauchy stress related to the viscous deformation of the slow relaxation can be derived from  $\Psi_s^v(\mathbf{F}_s^v, T)$  as:

$$\boldsymbol{\sigma}_s^{\text{ev}} = \frac{\mu_{sv}(T) \bar{\lambda}^v}{3J \bar{\lambda}_L} \mathfrak{L}^{-1} \left( \frac{\bar{\lambda}^v}{\bar{\lambda}_L} \right) (\mathbf{B}_s^v - (\bar{\lambda}^v)^2 \mathbf{I}) \quad (18)$$

where  $\mathbf{B}_s^v = \mathbf{F}_s^v \mathbf{F}_s^{vT}$  is the viscous left Cauchy-Green deformation tensor of the slow relaxation response.

The temperature dependence is included into the shear moduli of the fast response and the viscous contribution of the slow response to capture overall stiffness sensitivity with these variables:

$$\mu_f(T) = \mu_{f0} + m_1(T - T_0) \quad (19)$$

$$\mu_{sv}(T) = \mu_{sv0} + m_2(T - T_0) \quad (20)$$

where  $\mu_{f0}$  and  $\mu_{sv0}$  are the shear moduli at the reference temperature  $T_0$  of each relaxation response,  $m_1$  and  $m_2$  are temperature-sensitivity material parameters.

#### 4.4. Viscous flow rules

To complete the constitutive formulation of the model, we need to provide flow rules to govern the evolution of the viscous components of the deformation gradient. To this end, non-linear dashpots are defined for each relaxation response in the form of a potential function. The evolution of the viscous flow of the fast relaxation component is given by the following set of equations:

$$\mathbf{D}_f^v = \mathbf{F}_f^e \dot{\mathbf{F}}_f^v \mathbf{F}_f^{v-1} \mathbf{F}_f^{e-1} = \dot{\gamma}_f^v \mathbf{N}_f^v \quad (21)$$

with  $\mathbf{N}_f^v$  being a tensor describing the viscous flow direction, and  $\dot{\gamma}_f^v$  a viscous multiplier describing the viscous flow magnitude. These variables can be defined as:

$$\mathbf{N}_f^v = \frac{\boldsymbol{\sigma}_f^{\text{dev}}}{\sqrt{\boldsymbol{\sigma}_f^{\text{dev}} : \boldsymbol{\sigma}_f^{\text{dev}}}} \quad (22)$$

$$\dot{\gamma}_f^v = \dot{\gamma}_{f0} \left( \frac{\sqrt{\boldsymbol{\sigma}_f^{\text{dev}} : \boldsymbol{\sigma}_f^{\text{dev}}}}{\tau_f(T)} \right)^{nf} \quad (23)$$

where  $\dot{\gamma}_{f0}$  is a reference strain rate,  $nf$  is a strain rate sensitivity parameter, and  $\tau_f(T)$  is a temperature-dependent equivalent stress threshold defined as:

$$\tau_f(T) = \tau_{f0} e^{m_3 T} \quad (24)$$

with  $\tau_{f0}$  and  $m_3$  being material parameters.

The viscous flow rule of the slow relaxation response is described in the same manner but with  $\boldsymbol{\sigma}_s^{\text{flow}} = \boldsymbol{\sigma}_s - \boldsymbol{\sigma}_s^{\text{ev}}$  being the driving force governing the viscous flow:

$$\mathbf{D}_s^v = \mathbf{F}_s^e \dot{\mathbf{F}}_s^v \mathbf{F}_s^{v-1} \mathbf{F}_s^{e-1} = \dot{\gamma}_s^v \mathbf{N}_s^v \quad (25)$$

$$\mathbf{N}_s^v = \frac{(\boldsymbol{\sigma}_s^{\text{flow}})^{\text{dev}}}{\sqrt{(\boldsymbol{\sigma}_s^{\text{flow}})^{\text{dev}} : (\boldsymbol{\sigma}_s^{\text{flow}})^{\text{dev}}}} \quad (26)$$

$$\dot{\gamma}_s^v = \dot{\gamma}_{s0} \left( \frac{\sqrt{(\boldsymbol{\sigma}_s^{\text{flow}})^{\text{dev}} : (\boldsymbol{\sigma}_s^{\text{flow}})^{\text{dev}}}}{\tau_s} \right)^{ns} \quad (27)$$

where  $\dot{\gamma}_{s0}$ ,  $ns$ ,  $\tau_s$  are the corresponding material parameters. Note that  $\tau_s$  has been chosen independent of temperature for simplicity.

#### 5. Model calibration and results

In this section, we evaluate the model capability to capture the different mechanisms involved during the deformation process of PVDF. Note that the flow rules and temperature dependences shown in Eqs. (19), (20), (23), (24) and (27) have been chosen in rather simple forms (linear, simple potentials and exponentials) to simplify the model and reduce the number of parameters. In this regard, we distance our modelling efforts from describing the exact solution of the stress-strain curves by adding mathematical complexity into phenomenological formulations. On contrary, we aim at describing all

the different tendencies and material dependences observed in the experiments by simplified expressions.

First, the model is implemented within a numerical framework where the flow rules are computed by explicit integration algorithms and the evolution of the deformation gradient under compressible conditions is computed by an implicit integration algorithm (see *Appendix* for details). Then, the model parameters are identified by optimisation comparing model predictions and experimental results for a wide variety of loading conditions. The final set of parameters selected is presented in Table 1.

**Table 1:** Model parameters for PVDF.

Fast relaxation response						
$\mu_{f0}$ (MPa)	$m_1$ (MPa/K)	$\dot{\gamma}_{f0}$ ( $s^{-1}$ )	$\tau_{f0}$ (MPa)	$m_3$ ( $K^{-1}$ )	$nf$ (-)	
400	-5	0.001	280	-0.014	13	
Slow relaxation response						
$\mu_s$ (MPa)	$\mu_{sv}$ (MPa)	$m_2$ (MPa/K)	$\bar{\lambda}_L$ (-)	$\dot{\gamma}_{s0}$ ( $s^{-1}$ )	$\tau_s$ (MPa)	$ns$ (-)
3400	7	-0.3	2.5	0.001	7	50
General properties						
$\rho$ (kg/m <sup>3</sup> )	$C_p$ (J/Kg K)	$\theta_{ref}$ (K)	$\beta$ (-)	$K$ (GPa)		
1780	1600	293	0.8	1.22		

The model prediction for monotonic quasi-static conditions and different testing temperatures is shown in Figure 10. This figure presents the capability of the model to capture temperature dependence on the yield stress of the material: higher yield stress is reached when decreasing the testing temperature. Note that the model predictions differ for testing temperatures of -10°C and -20°C. This deviation in model predictions is due to the consideration of the simple expression used in Eq. (24). More complex expressions can be easily added here to capture the change in the temperature-dependent yield stress across glass transition (see works by Richeton et al. (2006) and Garcia-Gonzalez et al. (2020)). Moreover, the temperature dependence of the large deformation regime described in Eq. (20) can be observed in the curves for different testing temperatures. Here, lower values of temperature lead to a more concave stress-strain shape, indicating a reduction in polymeric chains mobility and thus a significant deformation hardening.

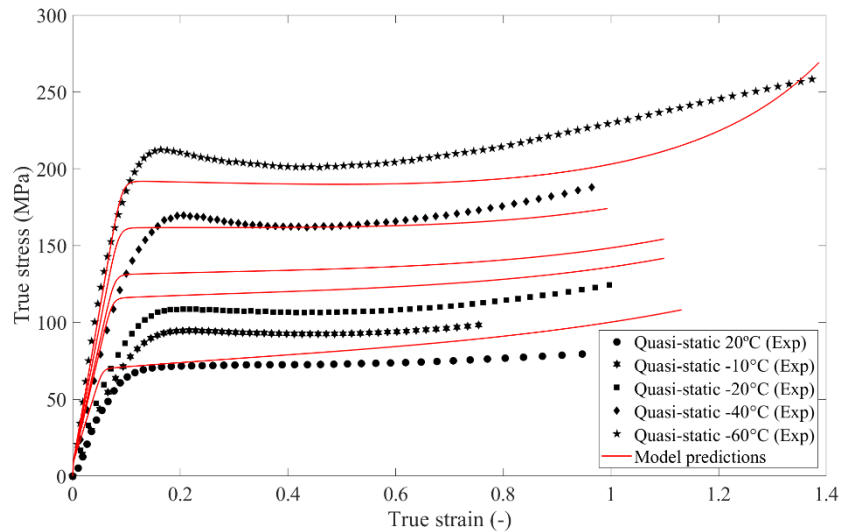


**Figure 10:** Comparison of model predictions and experimental data for compression quasi-static loading ( $0.001 \text{ s}^{-1}$ ) of PVDF at different temperatures: room,  $-10^\circ\text{C}$ ,  $-20^\circ\text{C}$ ,  $-40^\circ\text{C}$ ,  $-60^\circ\text{C}$ .

Cyclic loading tests were experimentally performed to study strain rate dependence within the low deformation rate regime as well as hysteresis. These experiments at  $0.01 \text{ s}^{-1}$  and different testing temperatures are compared with model predictions in Figure 11. Regarding temperature dependences, the observations mentioned before for monotonic loading also apply. In addition, it can be observed the capability of the model to predict the strain rate dependence on yield stress (note higher yield stresses with respect to experiments at  $0.01 \text{ s}^{-1}$ ). Moreover, the slow relaxation response of the material is appreciated during the hysteresis loops. In this regard, these simulations combine the fast response to capture instantaneous strain rate dependence in yielding; and the slow response to capture hysteresis, while incorporating temperature dependences in both of them.

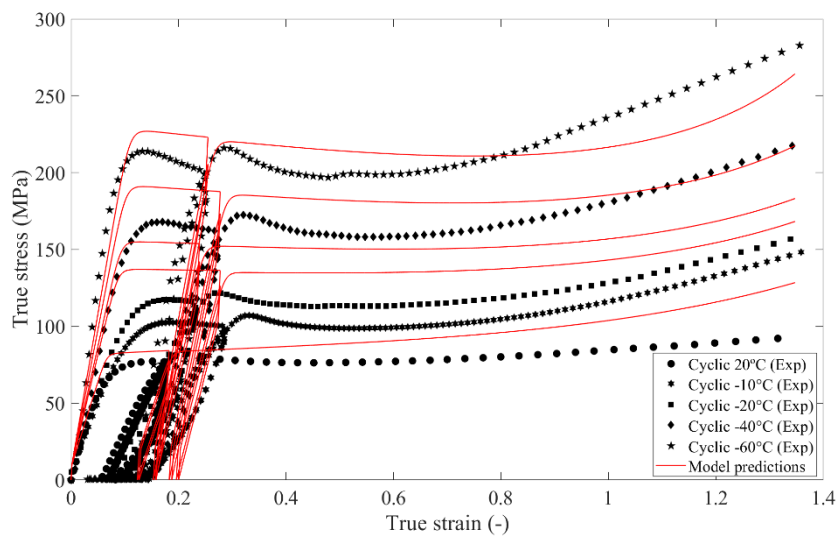


**Figure 11:** Comparison of model predictions and experimental data for cyclic loading ( $0.01 \text{ s}^{-1}$ ) of PVDF at different temperatures: room,  $-10^\circ\text{C}$ ,  $-20^\circ\text{C}$ ,  $-40^\circ\text{C}$ ,  $-60^\circ\text{C}$ .

The strain rate sensitivity can be further analysed by comparison of model predictions at higher deformation rates, i.e., SHPB tests. Figure 12 compares model predictions with experimental data for a wide range of loading conditions to present the capability of the model to accounts for different deformation mechanisms and material dependences at once. Here, we can observe the predictive capability of the model to capture yielding dependences. The model faithfully describes the increase of yield stress with strain rate (see model predictions for monotonic loading,  $0.001 \text{ s}^{-1}$ , cyclic loading,  $0.01 \text{ s}^{-1}$ , and SHPB dynamic loading,  $2000 \text{ s}^{-1}$ ). Furthermore, the model is able to describe slow relaxation responses leading to hysteresis from cyclic loading. Regarding the temperature dependences, the proposed model introduces such dependence on initial stiffness, yield stress and post-yield hardening. Higher yield stresses are obtained for lower testing temperatures as well as higher deformation hardening leading to a concave change in the flow stress evolution. In addition, the model reproduces the evolution of temperature due to inelastic dissipation, extremely relevant at high strain rates. This effect can be observed in the model prediction for SHPB tests at high temperature, where a continuous thermal softening is observed after yielding.

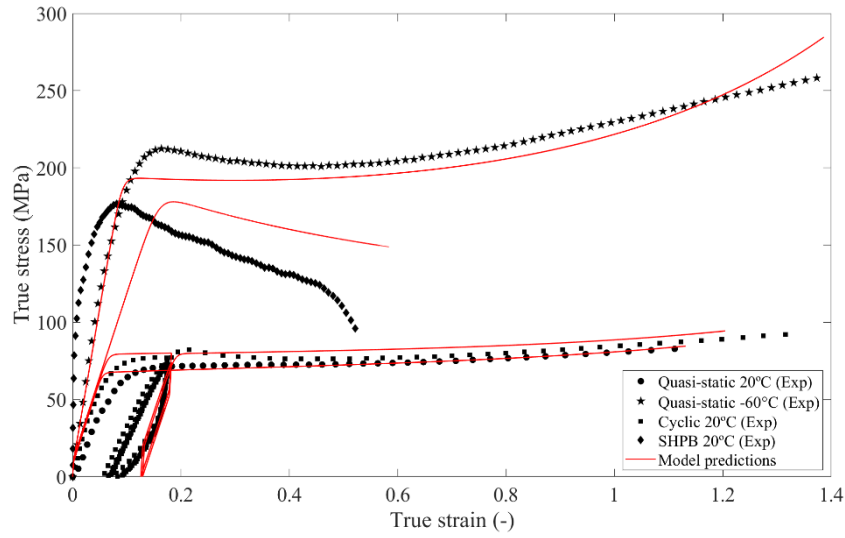


**Figure 12:** Comparison of model predictions and experimental data for different loading conditions: quasi-static monotonic loading ( $0.01 \text{ s}^{-1}$ ) at different testing temperatures; cyclic loading ( $0.01 \text{ s}^{-1}$ ); and dynamic loading (SHPB,  $2000 \text{ s}^{-1}$ ).

Although the proposed model can describe the different deformation mechanisms experimentally observed, there is still room for future avenues to improve the prediction accuracy. As mentioned before, the temperature-dependence on yield stress can be improved by adding more complex expressions into Eq. (24). Furthermore, although the yield stress and post-yield flow stress at high strain rates are well described, the model does not capture the stiffening effect within the linear region. To capture this, another viscoelastic constitutive branch representing a fast relaxation mechanism should be added, but an extra complexity in the model formulation would be necessarily introduced. Finally, the present model is restricted at high deformation rates as, to fully define the material response at the different testing temperatures, a brittle failure criterion should be added to capture material failure transitions due to microstructural changes across glass transition.

## 6. Conclusions

This work studies the mechanical behaviour of PVDF combining experimental and numerical methods. The study primarily focuses on the mechanical response of this polymer at low temperatures and a wide variety of loading conditions. The experimental characterisation first evaluates potential effects of thermal history by application of various cryogenic pre-treatments. This analysis identifies that the previous thermal history of the PVDF at low temperatures, even going across its glass transition, does not significantly affect its mechanical performance. These tests are performed for quasi-static, cyclic and dynamic loading conditions. Then, the mechanical behaviour of PVDF is tested at different loading conditions and testing temperatures ranging from room temperature to  $-60^\circ\text{C}$ . This study provides a complete view of the deformation and failure mechanisms of PVDF at: monotonic quasi-static loading conditions, cyclic loading conditions, and dynamic loading conditions. These results show a strong dependence of PVDF on testing temperature and strain rate, presenting a significant stiffening for lower temperatures and higher strain rates. These dependences are found to present a change in tendency at glass transition. In addition, a drastic change in failure mode is observed when going across glass transition temperature, going from a ductile response above this threshold to a brittle response below it. Then, all the experimental results are used to motivate the formulation of a new constitutive model to

describe the main dependences observed. The formulation of the model relies on a finite deformation framework that satisfies the thermodynamic principles and accounts temperature dependences, strain rate sensitivity and hysteresis. The proposed model is implemented, and we provide calibration of its parameters for PVDF. The calibrated model shows a good capability to describe all the different deformation mechanisms observed from the experiments. Finally, the limitations of the model and future guidance to overcome them are discussed in detail. Overall, we provide a new modelling tool to predict the response of PVDF under a wide range of room-to-low temperature loading conditions. These results, along with future extensions of 3D printed polymeric modelling (Garzon-Hernandez et al., 2020), aim at serving as basis for new avenues in 3D printed responsive components as sensor-actuator systems.

**Acknowledgements:** The authors acknowledge support from Ministerio de Ciencia, Innovación y Universidades, Agencia Estatal de Investigación y Fondo Europeo de Desarrollo Regional, como entidades financiadoras (RTI2018-094318-B-I00). D.G.-G., S.G.-H. and A.A. acknowledge support from Programa de Apoyo a la Realización de Proyectos Interdisciplinarios de I+D para Jóvenes Investigadores de la Universidad Carlos III de Madrid (BIOMASKIN-CM-UM3M). D.G.-G. acknowledges support from the Talent Attraction grant (CM 2018 - 2018-T2/IND-9992) from the Comunidad de Madrid.

## Appendix: Numerical implementation of compressible deformation

This appendix summarises the formulation and implementation of the deformation gradient evolution under compressible conditions. For uniaxial conditions and assuming isotropic behaviour for the PDVF, the next conditions must be fulfilled:

$$Residual = \sigma_{22} = \sigma_{33} = 0 \quad (A.1)$$

$$\lambda_{22} = \lambda_{33} \quad (A.2)$$

These constraints are imposed by computing an incremental iterative Newton-Raphson method:

$$\lambda_{2(n+1)} - \lambda_{2(n)} + \frac{\sigma_{F22}(\lambda_{2(n)})}{\sigma'_{F22}(\lambda_{2(n)})} = 0 \quad (A.3)$$

$$\text{where } \sigma'_{F22}(\lambda_{2(n)}) = \frac{\partial \sigma_{F22}}{\partial \lambda_2}.$$

The definition of  $\sigma_{F22}$  in terms of principal stretches is obtained through the definition of the total stress expressed in terms of principal stretches. Starting from Eq. (1):

$$\boldsymbol{\sigma} = K(J - 1)\mathbf{I} + \frac{\mu_f(T)}{J}(\mathbf{B}_f^e)^{\text{dev}} + \frac{\mu_s(T)}{J}(\mathbf{B}_s^e)^{\text{dev}} \quad (A.4),$$

$\sigma_{22}$  can be written in terms of the components  $B_{f22}^e$  and  $B_{s22}^e$ , which can be defined in terms of principal stretches as:

$$(\mathbf{B}_{f22}^e)^{\text{dev}} = \frac{\lambda_2^2}{\lambda_1^{2/3}\lambda_2^{4/3}F_{f22}^2} - \frac{1}{3}\left[\frac{\lambda_1^2}{\lambda_1^{2/3}\lambda_2^{4/3}F_{f11}^2} + \frac{2\lambda_2^2}{\lambda_1^{2/3}\lambda_2^{4/3}F_{f22}^2}\right] \quad (A.5)$$

$$(\mathbf{B}_{s22}^e)^{\text{dev}} = \frac{\lambda_2^2}{\lambda_1^{2/3}\lambda_2^{4/3}F_{s22}^2} - \frac{1}{3}\left[\frac{\lambda_1^2}{\lambda_1^{2/3}\lambda_2^{4/3}F_{s11}^2} + \frac{2\lambda_2^2}{\lambda_1^{2/3}\lambda_2^{4/3}F_{s22}^2}\right] \quad (A.6)$$



In the same manner,  $\frac{(B_{f22}^e)^{dev}}{J}$  and  $\frac{(B_{s22}^e)^{dev}}{J}$  are defined as:

$$\frac{(B_{f22}^e)^{dev}}{J} = \frac{1}{\lambda_1^{5/3}\lambda_2^{4/3}F_{f22}^v} - \frac{1}{3}\left[\frac{\lambda_1^{1/3}}{\lambda_2^{10/3}F_{f11}^v} + \frac{2}{\lambda_1^{5/3}\lambda_2^{4/3}F_{f22}^v}\right] \quad (A.7)$$

$$\frac{(B_{s22}^e)^{dev}}{J} = \frac{1}{\lambda_1^{5/3}\lambda_2^{4/3}F_{s22}^v} - \frac{1}{3}\left[\frac{\lambda_1^{1/3}}{\lambda_2^{10/3}F_{s11}^v} + \frac{2}{\lambda_1^{5/3}\lambda_2^{4/3}F_{s22}^v}\right] \quad (A.8)$$

Finally,  $\sigma_{F22}$  and its derivative with respect to  $\lambda_2$  read as:

$$\sigma_{F22} = K(J-1) + \mu_f(T)\left[\frac{1}{3\lambda_1^{5/3}\lambda_2^{4/3}F_{f22}^v} - \frac{1}{3}\left[\frac{\lambda_1^{1/3}}{\lambda_2^{10/3}F_{f11}^v}\right]\right] + \mu_s(T)\left[\frac{1}{3\lambda_1^{5/3}\lambda_2^{4/3}F_{s22}^v} - \frac{1}{3}\left[\frac{\lambda_1^{1/3}}{\lambda_2^{10/3}F_{s11}^v}\right]\right] \quad (A.9)$$

$$\frac{\partial \sigma_{F22}}{\partial \lambda_2} = 2K\lambda_1\lambda_2 + \mu_f(T)\left[\frac{4}{9\lambda_1^{5/3}\lambda_2^{1/3}F_{f22}^v} - \frac{10}{9}\left[\frac{\lambda_1^{1/3}}{\lambda_2^{7/2}F_{f11}^v}\right]\right] + \mu_s(T)\left[\frac{4}{9\lambda_1^{5/3}\lambda_2^{1/3}F_{s22}^v} - \frac{10}{9}\left[\frac{\lambda_1^{1/3}}{\lambda_2^{7/2}F_{s11}^v}\right]\right] \quad (A.10)$$

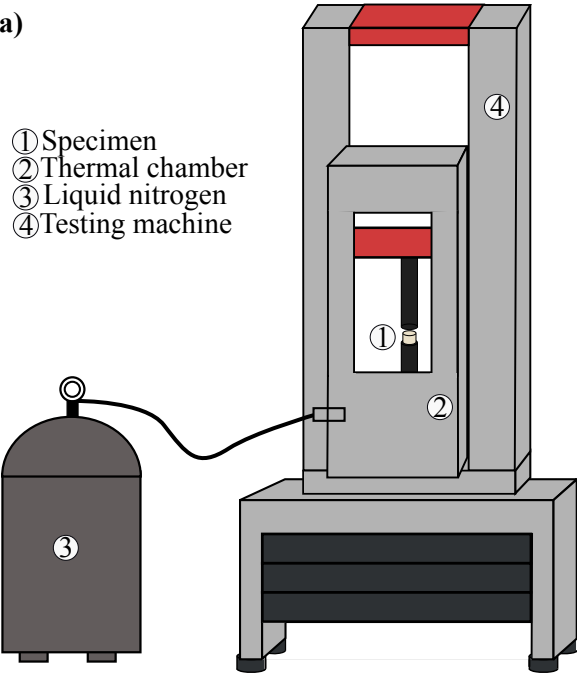
## REFERENCES

- Baldissera, P., Delprete, C., 2013. Current and Potential Applications of Cryogenic Treated Polymers. In: Kalia S., Fu SY. (eds) Polymers at Cryogenic Temperatures. Springer, Berlin, Heidelberg.
- Barba, D., Arias, A., Garcia-Gonzalez, D., 2020. Temperature and strain rate dependences on hardening and softening behaviours in semi-crystalline polymers: Application to PEEK, International Journal of Solids and Structures, 182–183: 205-217.
- Castagnet, S., Gacougnolle, J.-L., Dang, P., 2000. Correlation between macroscopical viscoelastic behaviour and micromechanisms in strained  $\alpha$  polyvinylidene fluoride (PVDF), Materials Science and Engineering A, 276: 152-159.
- Coleman, B.D., Gurtin, M.E., 1967. Thermodynamics with internal state variables, J. Chem. Phys., 47: 597.
- Coleman, B.D., Noll, W., 1963. The thermodynamics of elastic materials with heat conduction and viscosity, Arch. Ration. Mech. Anal., 13: 167-178.
- Dargaville, T.R., Celina, M., Chaplya, P.M., 2005. Evaluation of piezoelectric Poly(vinylidene fluoride) polymers for use in space environments. I. Temperature limitations, Journal of Polymer Science: Part B: Polymer Physics, 43: 1310-1320.
- Eddiai, A., Meddad, M., Farhan, R., Mazroui, M., Rguiti, M., Guyomar, D., 2019. Using PVDF piezoelectric polymers to maximize power harvested by mechanical structure, Superlattices and Microstructures 127: 20-26.
- Feng, J., Xuan, S., Ding, L., Gong, X., 2017. Magnetoactive elastomer/PVDF composite film based magnetically controllable actuator with real-time deformation feedback property, Composites Part A: Applied Science and Manufacturing, 103: 25-34.
- Friedrich, K., 2018. Polymer composites for tribological applications, Advanced Industrial and Engineering Polymer Research, 1: 3-39.

- Garcia-Gonzalez, D., 2019. Magneto-visco-hyperelasticity for hard-magnetic soft materials: theory and numerical applications. *Smart Materials and Structures*, 28(085020).
- Garcia-Gonzalez, D., Jayamohan, J., Sotiropoulos, S.N., Yoon, S.-H., Cook, J., Siviour, C.R., Arias, A., Jérusalem, A., 2017. On the mechanical behaviour of PEEK and HA cranial implants under impact loading. *Journal of the Mechanical Behavior of Biomedical Materials*, 69: 342-354.
- Garcia-Gonzalez, D., Jérusalem, A., 2019. Energy based mechano-electrophysiological model of CNS damage at the tissue scale. *Journal of the Mechanics and Physics of Solids*, 125: 22-37.
- Garcia-Gonzalez, D., Rusinek, A., Bendarma, A., Bernier, R., Klosak, M., Bahi, S., 2020. Material and structural behaviour of PMMA from low temperatures to over the glass transition: Quasi-static and dynamic loading, *Polymer Testing*, 81:106263.
- Garcia-Gonzalez, D., Landis, C.M., 2020. Magneto-diffusion-viscohyperelasticity for magneto-active hydrogels: rate dependences across time scales, *Journal of the Mechanics and Physics of Solids*, 103934, DOI: <https://doi.org/10.1016/j.jmps.2020.103934>.
- Garcia-Gonzalez, D., Zaera, R., Arias, A., 2017. A hyperelastic-thermoviscoplastic constitutive model for semi-crystalline polymers: application to PEEK under dynamic loading conditions. *International Journal of Plasticity*, 88:27-52.
- Garzon-Hernandez, S., Garcia-Gonzalez, D., Jerusalem, A., Arias, A., 2020. Design of FDM 3D printed polymers: an experimental-modelling methodology for mechanical properties prediction, *Materials and Design*, 188:108414.
- Haddadi, S.A., Ghaderi, S., Amini, M., Ramazani, S.A.A., 2018. Mechanical and piezoelectric characterizations of electrospun PVDF-nanosilica fibrous scaffolds for biomedical applications, *Materials Today: Proceedings*, 5: 15710-15716.
- Kim, Y., Yuk, H., Zhao, R., Chester, S.A., Zhao, X., 2018. Printing ferromagnetic domains for untethered fast-transforming soft materials, *Nature* 558: 274–9.
- Laiarinandrasana, L., Besson, J., Lafarge, M., Hochstetter, G., 2009. Temperature dependent mechanical behaviour of PVDF: Experiments and numerical modelling, *International Journal of Plasticity*, 25: 1301-1324.
- Li, W., Gazonas, G., Brown, E.N., Rae, P.J., Negahban, M., 2019. Thermomechanical model for monotonic and cyclic loading of PEEK, *Mechanics of Materials*, 129: 113-138.
- Li, L., Zhang, M., Rong, M., Ruan, W., 2014. Studies on the transformation process of PVDF from  $\alpha$  to  $\beta$  phase by stretching, *RSC Adv.* 4(8): 3938.
- Liao, Z., Hossain, M., Yao, X., Mehnert, M., Steinmann, P., 2020. On thermo-viscoelastic experimental characterization and numerical modelling of VHB polymer, *International Journal of Non-Linear Mechanics*, 118: 103263.
- Motta, E.P., Reis, J.M.L., da Costa Mattos, H.S., 2018. Analysis of the cyclic tensile behaviour of an elasto-viscoplastic polyvinylidene fluoride (PVDF), *Polymer Testing* 67: 503-512.
- Park, C., Ounaies, Z., Wise, K.E., Harrison, J.S., 2004. In situ poling and imidization of amorphous piezoelectric polyimides, *Polymer*, 45: 5417-5425.
- Richeton, J., Ahzi, S., Vecchio, K.S., Jiang, F.C., Adharapurapu, R.R., 2006. Influence of temperature and strain rate on the mechanical behavior of three amorphous polymers: characterization and modeling of the compressive yield stress, *Int. J. Solids Struct.*, 43 (7–8): 2318-2335.

- Ruan, L., Yao, X., Chang, Y., Zhou, L., Qin, G., Zhang, X., 2018. Properties and Applications of the  $\beta$  Phase Poly(vinylidene fluoride), *Polymers* 10(3): 228.
- Santimetaneedol, A., Tripuraneni, R., Chester, S.A., Nadimpalli, S.P.V., 2016. Time-dependent deformation behavior of polyvinylidene fluoride binder: implications on the mechanics of composite electrodes, *Journal of Power Sources*, 332: 118-128.
- Scalet, G., Pandini, S., Messori, M., Toselli, M., Auricchio, F., 2018. A one-dimensional phenomenological model for the two-way shape-memory effect in semi-crystalline networks, *Polymer* 158: 130-148.
- Schuhler, E., Coppalle, A., Vieille, B., Yon, J., Carpier, Y., 2018. Behaviour of aeronautical polymer composite to flame: A comparative study of thermoset- and thermoplastic-based laminate, *Polymer Degradation and Stability* 152: 105-115.
- Shen, F., Kang, G., Lam, Y.C., Liu, Y., Zhou, K., 2019. Thermo-elastic-viscoplastic-damage model for self-heating and mechanical behavior of thermoplastic polymers, *International Journal of Plasticity*, 121: 227-243.
- Singh, R.K., Lye, S.W., Miao, J., 2020. Measurement of impact characteristics in a string using electrospun PVDF nanofibers strain sensors, *Sensors and Actuators A: Physical*, 303: 111841.
- Siviour, C.R., Walley, S.M., Proud, W.G., Field, J.E., 2005. The high strain rate compressive behaviour of polycarbonate and polyvinylidene difluoride, *Polymer* 46: 12546-12555.
- Tarbuttona, J., Leb, T., Helfrichb, G., Kirkpatrickb, M., 2017. Phase Transformation and Shock Sensor Response of Additively Manufactured Piezoelectric PVDF, *Procedia Manufacturing*, 10: 982-989.
- Vinogradov, A.M., Schmidt, V.H., Tuthill, G.F., Bohannon, G.W., 2004. Damping and electromechanical energy losses in the piezoelectric polymer PVDF, *Mechanics of Materials*, 36: 1007-1016.
- Whatmore, R.W., 1991. Piezoelectric and Pyroelectric Materials and Their Applications. In: Miller L.S., Mullin J.B. (eds) *Electronic Materials*, Springer, Boston, MA.
- Yang, Y., Pan, H., Xie, G., Jiang, Y., Chen, C., Su, Y., Wang, Y., Tai, H., 2020. Flexible piezoelectric pressure sensor based on polydopamine-modified BaTiO<sub>3</sub>/PVDF composite film for human motion monitoring, *Sensors and Actuators A: Physical*, 301: 111789.
- Yu, C., Kang, G., Chen, K., Lu, F., 2017. A thermo-mechanically coupled nonlinear viscoelastic-viscoplastic cyclic constitutive model for polymeric materials, *Mechanics of Materials*, 105: 1-15.
- Zhang, J., Liu, D., Han, Q., Jiang, L., Shao, H., Tang, B., Lei, W., Lin, T., Wang, C.H., 2019. Mechanically stretchable piezoelectric polyvinylidene fluoride (PVDF)/Boron nitride nanosheets (BNNs) polymer nanocomposites, *Composites Part B: Engineering*, 175: 1359-8368.
- Zhao, Y., Zhang, Y., Xu, J., Zhang, M., Yu, P., Zhao, Q., 2020. Frequency domain analysis of mechanical properties and failure modes of PVDF at high strain rate, *Construction and Building Materials*, 235: 0950-0618.

a)



- ① Specimen
- ② Thermal chamber
- ③ Liquid nitrogen
- ④ Testing machine

b)

- ① Specimen
- ② Incident bar
- ③ Transmitted bar
- ④ Thermal chamber
- ⑤ Liquid nitrogen
- ⑥ Thermocouple

